Observing System Simulation Experiment: Development of the system and preliminary results

Shu-Hua Chen,[1,2] Jhih-Ying Chen,[3] Wei-Yu Chang,[3] Pay-Liam Lin,[3] Po-Hsiung Lin,[4] and Wen-Yih Sun[2,5]

Received 22 September 2010; revised 20 March 2011; accepted 7 April 2011; published 2 July 2011.

[1] An Observing System Simulation Experiment (OSSE) was developed and conducted to assess the potential impact of different observing strategies of field experiments on analysis and short-term forecasts. A Mei-Yu front rainfall case study, occurring in 2003 in southeastern Asia, was utilized to demonstrate the OSSE application to field experiments. Data sampling strategies from the Taiwan Island Monsoon Rainfall Experiment (TIMREX), with some modifications, were used. The nature run was produced by the Weather Research and Forecasting (WRF) model with a resolution of 1 km. The observational operators, which were developed to simulate observations, included radar, radiosonde, dropsonde, wind profiler, and surface stations. The verification of simulated observations, such as radar echo and radial velocity, and preliminary results from data assimilation experiments, demonstrated that the developed OSSE system performed reasonably well. The use of more observations, such as radar data, dropsondes, and extra radiosondes, was able to significantly improve analysis of winds and, to a lesser extent, moisture, and short-term rainfall forecasts. While more observations helped improve simulations, the use of higher-frequency observations (e.g., 3 h radiosondes) launched at the same locations for this case study did not substantially influence results. Thus, the information may be potentially saturated and more studies to tackle this problem are required.

Citation: Chen, S.-H., J.-Y. Chen, W.-Y. Chang, P.-L. Lin, P.-H. Lin, and W.-Y. Sun (2011), Observing System Simulation Experiment: Development of the system and preliminary results, *J. Geophys. Res.*, *116*, D13202, doi:10.1029/2010JD015103.

1. Introduction

[2] Hurricanes/typhoons, fronts, and other severe storms are life-threatening weather-related disasters. Each year, the worldwide loss of lives and property damage due to these disasters is significant. Besides the original severity of those weather systems, their interaction with steep terrain (e.g., the Rocky Mountains and Sierra Nevada Mountains in the U.S. and the Central Mountain Ridge in Taiwan) makes their behavior more complicated and extreme. The prediction of these systems often becomes more difficult if the systems propagate from water surfaces (e.g., the southwest monsoonal flow from the South China Sea to Taiwan), where oceans are the main supply of moisture and heat to the systems and where observations are potentially sparse.

[3] In general, conventional observations, such as surface stations and upper air soundings, are insufficient to depict atmospheric conditions when studying detailed dynamical and physical processes of severe weather systems; this is especially true for observations over oceans and mountainous regions. Satellite observations can potentially describe the atmosphere in more detail; however, data are sometimes limited to low temporal frequency (e.g., twice a day for polar-orbiting satellites), to low vertical spatial resolution, or by cloud contamination. Therefore, special field experiments, such as CALJET (California Land-Falling Jets Experiment) [*Ralph et al.*, 1999], PACJET (Pacific Coastal Jets Experiment) [*White et al.*, 2002], IMPROVE (Improvement of Microphysical Parameterization through Observational Verification Experiment) [*Stoelinga et al.*, 2003], and MAP (Mesoscale Alpine Programme) [*Bougeault et al.*, 2001], have been conducted to intensively collect atmospheric information to improve forecasting and advance our understanding of dynamical and physical processes of precipitation systems over mountainous regions. Some progress has been made [*Neiman et al.*, 2004; *Ralph et al.*, 2004; *Jiang and Doyle*, 2004; *Davis et al.*, 2004; *Garvert et al.*, 2005;

[1]Department of Land, Air, and Water Resources, University of California, Davis, California, USA.
[2]National Typhoon and Flood Research Institute, Taipei, Taiwan.
[3]Department of Atmospheric Sciences, National Central University, Chung-Li, Taiwan.
[4]Department of Atmospheric Sciences, National Taiwan University, Taipei, Taiwan.
[5]Department of Earth and Atmospheric Sciences, Purdue University, West Lafayette, Indiana, USA.

0148-0227/11/2010JD015103

Houze and Medina, 2005; *Evans et al.*, 2005; *Woods et al.*, 2005; *Ralph et al.*, 2005; *Neiman et al.*, 2006; *Garvert et al.*, 2007; *Yu et al.*, 2007], but many unknowns remain.

[4] For any field experiment, data collecting strategies designed with the use of different instruments are crucial to the success of the project since budgets are usually limited and some instruments are nonreusable (e.g., radiosondes and dropsondes). Therefore, to maximize the improvement in forecasts, instruments should be deployed at locations where observations (i.e., targeted observations) have the strongest influence on weather forecasts, namely to improve initial conditions most effectively. In general, two numerical techniques have been applied to potentially identify those most sensitive locations/regions. One is a forward numerical technique and the other is a singular vector technique [*Palmer et al.*, 1998]. The forward method perturbs one variable at one model grid point each time in initial conditions, iterating over variables and grid points. After examining every variable at every grid point, the locations where initial perturbations on particular variables give the most significant change in forecasting are targeted for observations to be collected. Alternatively, the singular vector method uses a forward and an adjoint model to identify the most sensitive areas for data collection. The results from the latter method can be sensitive to the definition of the response function. Nevertheless, the adjoint backward method (i.e., the singular vector technique) is computationally much more efficient than the forward method, and it has been successfully used in field experiments [*Gelaro et al.*, 2002; *Aberson*, 2003; *Majumdar et al.*, 2006; *Wu et al.*, 2005, 2007a, 2007b].

[5] However, sometimes the deployments of instruments are constrained to certain regions or to preferred potential locations (e.g., after site survey) due to limitations of the environment. In such situations, the adjoint backward method might not be suitable since the most sensitive (i.e., targeted) areas may not be within those accessible regions or preselected potential locations. In contrast, under such constraints the forward method is more applicable because there are usually few potential observational locations to be tested and the computational cost is thus relatively cheap. Given these considerations, an Observing System Simulation Experiment (OSSE) can be applied to effectively test proposed observing strategies (or targets) using the forward approach before a field experiment takes place. Although the OSSE methodology is not perfect, it should provide valuable information for the design of field projects.

[6] An OSSE system is constituted by a nature run (i.e., an approximate atmosphere), simulated observations, and data assimilation experiments which are used to evaluate the simulated observations. The nature run is usually from a high-resolution state-of-science model forecast, and is used to create observations and validate data assimilation experiments. OSSE has many applications [*Kuo and Anthes*, 1984; *Daley and Mayer*, 1986; *Chang and Holt*, 1994; *Atlas*, 1997; *Brewster*, 2003; *Davolio and Buzzi*, 2004; *Keil*, 2004; *Tong and Xue*, 2005; *Xue et al.*, 2006; *Masutani et al.*, 2010], such as assessing future satellite observations on modeling weather systems and analysis [*Lahoz et al.*, 2005; *Stoffelen et al.*, 2006; *Masutani et al.*, 2010], or determining the needed temporal and/or spatial resolutions in a synoptic network for trajectory calculations [*Kuo et al.*, 1985], and error growth studies [*Warner et al.*, 1989]. *Kuo et al.* [1985] found that the synoptic network over North America was not sufficient for trajectory studies, and it was more cost effective to increase the observational frequency than to increase the spatial resolution.

[7] In an idealized, high-resolution (1~2 km) numerical setting, *Tong and Xue* [2005] and *Xue et al.* [2006] used OSSE to examine a data assimilation system, which was based on ensemble (ensemble square root for *Xue et al.* [2006]) Kalman filtering, and to evaluate the impact of radar data on supercell studies. They found that when assimilating data from a short-range radar alone, errors can develop in the analysis if the radar only partially covers the weather system. In their study, more realistic observations were simulated as data were sampled on radar elevation levels with a consideration of the Earth curvature effect and atmospheric refractivity. However, the sedimentation of hydrometeors, which is included in real radar observations, was excluded in both simulated radial velocity and the data assimilation system. Moreover, the same numerical model was used for both the nature run and the data assimilation experiments, i.e., the identical twin problem.

[8] In addition to the applications mentioned above, OSSE can potentially be an excellent tool for designing and evaluating a field project, and can inform decisions on how to integrate different instruments, where to place instruments, how frequently to deploy instruments, etc. Moreover, OSSE can be used to detect if the observed information is saturated and, therefore, that additional instruments in time or space may not provide much further information. In this study, an OSSE was developed to demonstrate the practices of the OSSE application to field experiments. A Mei-Yu front rainfall event that occurred around the Taiwan area in 2003 was used for the demonstration. Instead of using an idealized scenario, data sampling strategies from the Taiwan Island Monsoon Rainfall Experiment (TIMREX), with some modifications, were adopted for investigation. The impact of simulated observations from different sampling strategies on analysis and short-term forecasts was assessed.

[9] TIMREX, a joint field project among several countries, sampled the heavy rainfall environment over southwestern Taiwan during the Mei-Yu season in May and June from 2008 to 2010. Taiwan is an island located in the southwestern Pacific Ocean and has a size of about 200 km and 400 km in the east-west and south-north directions, respectively. The island has 100 mountains which are higher than 3 km and the peak of the Central Mountain Ridge (CMR) is about 4 km. With such a complex topography, Taiwan experiences heavy orographic rainfall from different weather systems, including stationary fronts, southwesterly flows, and mesoscale circulation during the Mei-Yu season. The interaction between those frontal systems and the complex terrain creates interesting convective systems. However, a lack of data prevents scientists from understanding these severe weather systems. The purpose of this study is not to investigate the dynamical and physical processes of the Mei-Yu front systems, but to use data sampling strategies similar to TIMREX for a demonstration of the OSSE application for field experiments.

[10] This paper is organized as follows. The OSSE system, numerical modeling, and observational operators are introduced in section 2. The design of the nature run and simulated observations are described in section 3. Data assimilation experiments and preliminary results are pre-

sented in section 4, and concluding remarks are given in section 5.

2. Methodology, Numerical Modeling, and Observational Operators

2.1. Observing System Simulation Experiment

[11] Figure 1 shows the flowchart of the OSSE study. The nature run was produced by the Weather Research and Forecasting (WRF) model with a resolution of 1 km. The nature run and developed observational operators (see section 2.3) were used to create observations. Both existing and additional instruments for TIMREX are shown in Table 1 and Figure 2. Note that since the primary interest is short-term rainfall forecasts over Taiwan, only instruments from Taiwan and TIMREX were considered. Moreover, a few additional instruments in TIMREX that became available after this OSSE study was conducted, such as a radar from Japan, were excluded. The existing instruments included four radars from the Central Weather Bureau (CWB), one wind profiler from the Environmental Protection Agency (EPA), four radiosondes, and thirty-three surface stations in Taiwan. The additional instruments that were not available on a regular observing basis included the S-Band Polarization (S-POL) radar from the National Center for Atmospheric Research (NCAR), the Taiwan Experimental Atmospheric Mobile–Radar (TEAM-R), one Integrated Sounding System (ISS) wind profiler from the National Central University (NCU) in Taiwan, eight radiosondes, and many dropsondes deployed from an ASTRA jet aircraft along a 14 km ceiling height.

[12] Observations were simulated for a 6 h time period for data assimilation experiments (see section 3). For simplicity, except for dropsondes, all observations were created off-line using the WRF instantaneous outputs from the nature run at exact hours (i.e., 0 h, 1 h, etc.). For dropsondes, the instruments are usually deployed from flights progressively in time when sampling data in the air. The receiver that was used in TIMREX can operate four sondes simultaneously and the temporal resolution for dropsondes can be as high as a few minutes. Therefore, the observational operator (i.e., observation simulator) for dropsondes was implemented within the WRF model, and each sounding was sampled sequentially as the model integrated forward with time (i.e., varying in time). Random errors were added into simulated observations that were then assessed in data assimilation experiments. Data assimilation analysis and short-term rainfall forecasts were compared with the true atmosphere (i.e., the nature run) to preliminarily evaluate different data sampling strategies used in TIMREX, with some modifications.

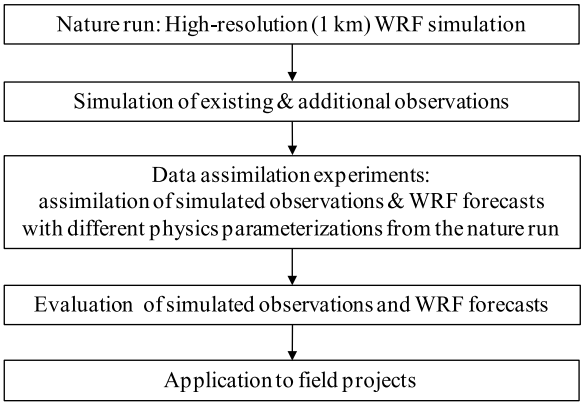

Figure 1. The flowchart of the OSSE study.

Table 1. Existing and Additional Observational Instruments for the OSSE Study[a]

Instruments (Number)	Symbol (Location)
Existing Observational Instruments	
Radiosondes (4)	S1 (Ban-Chiao), S2 (Hua-Lian), S3 (Ma-Kung), S4 (Green Island)
Surface stations (33)	Dots in Figure 2
Radars (4)	R1 (Wu-Fen-San), R2 (Ken-Ting), R3 (Hua-Lian), R4 (Chi-Gui)
Wind profiler (1)	W1 (EPA)
Additional Observational Instruments	
Radiosondes (8)	S5 (Tai-Chung), S6 (Tai-Nan), S7 (Ping-Tong), S8 (Heng-Chun), S9 (NCU), S10 (Dong-Sa), S11 (Ship1), S12 (Ship 2)
Radar (2)	R5 (S-POL) and R6 (TEAM-R)
Wind profiler (1)	W2 (ISS)
Dropsondes	Dots in Figure 8

[a]The symbols (e.g., S1, R1) and locations of each instrument are shown in Figure 1.

[13] When designing OSSEs, one should avoid the identical twin problem, in which both the nature run and data assimilation experiments use exactly the same numerical model and, by extension, include the use of similar initial and boundary conditions. Under the identical twin scenario, the numerical model becomes perfect (i.e., no model errors); this is counter to what happens in reality (i.e., models are never perfect) and will overestimate the impact of observations on model forecasts. Although the same numerical model (i.e., WRF) was used for both the nature run and the data assimilation experiments in this study, two primary approaches were used to reduce the identical twin problem. One is that global reanalysis, instead of degraded meteorological fields from the 18 h nature run, were used as the first guess for data assimilation experiments. The other is that most physics schemes that were used in data assimilation experiments differed from those used in the nature run. The use of different physics schemes can produce significant model errors for the OSSE study [*Meng and Zhang*, 2007], and this can effectively reduce the identical twin problem. In addition, the finest horizontal resolution in the nature run was higher than that in data assimilation experiments (1 km versus 3 km). This helps differentiate the nature run from data assimilation experiments (e.g., smoothed terrain in 3 km resolution), though the effect is relatively minor. Boundary conditions can also contribute to the identical twin problem. Although the same boundary conditions were used in the nature run and data assimilation experiments, the primary interests are the data assimilation analysis and the first 6 h rainfall forecasts. For such short-time integrations, forecasts are dominated by initial conditions instead of the boundary conditions. Therefore, the identical twin problem caused by the boundary conditions should be negligible in this study.

2.2. Weather Research and Forecasting Model and Its Variational Data Assimilation System

[14] The Advanced Research WRF (ARW) model version 2.2 [*Skamarock et al.*, 2005] was adopted for the OSSE study. The

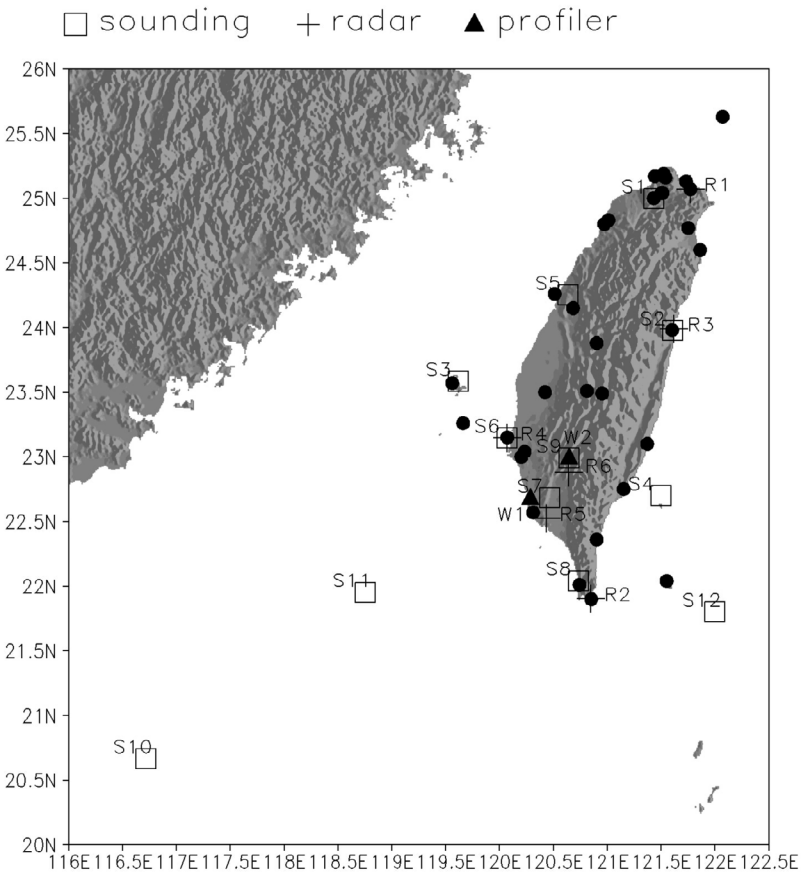

Figure 2. Types and locations of different instruments for the OSSE study (see Table 1 for each instrument).

ARW model is a compressible, three-dimensional, nonhydrostatic model using terrain-following mass coordinates and its governing equations are written in flux form. The Runge-Kutta third-order time scheme was employed and fifth- and third-order advection schemes were chosen for the horizontal and vertical directions, respectively. More information about the WRF model is available at http://www.wrf-model.org.

[15] The WRF variational data assimilation system (WRF Var) is capable of assimilating all the observations that were examined in this study. The observational errors and quality controls in the WRF Var system were applied directly. Due to the use of the high resolution model configuration for data assimilation experiments, the background error covariances for each domain (See section 4 for domain settings) were calculated from one month of daily WRF forecasts for initial times at 0000 and 1200 UTC in June 2003. The National Meteorological Center (NMC) method [*Parrish and Derber*, 1992] in the WRF Var package was adopted for background error calculations and a total of 60 members were used.

2.3. Development of Operators for Simulating Observations

[16] Observational operators (i.e., observation simulators) for each instrument were developed to simulate observations. Most operators were developed to mimic the procedure of their measurements in the real world. For example, the vertical sampling of a radiosonde/dropsonde sounding was not taken from a fixed vertical column but drifted horizontally across model grid points due to winds, while it was treated as column data when assimilated in a data assimilation system, as is usually performed. Therefore, some inherent errors that were associated with retrieval algorithms or the inconsistency of observational operators between observation simulation and data assimilation were included in this simulation study, as in reality. In addition, random perturbations, which were created using observational error covariance in WRF Var under the assumption of a zero mean error, were added to each simulated data to take into account the observational errors. However, errors due to instrument biases (e.g., dry biases in radiosondes and dropsondes) were ignored here. Below are brief descriptions of the operators for each instrument.

2.3.1. Radar

[17] All radars used here are in S band, except TEAM-R, which is in X band. The radar operator used to simulate observations has a resolution of 1 degree beam width and 1 km in the gate direction. Nine scanning elevation angles, such as 0.5, 1.5, 2.4, 3.3, 4.3, 6.0, 9.9, 14.6, and 19.5 degrees, were configured for all simulated radar observations. The scanning angle is defined as the angle between the radar beam and the horizon. The curvature effect of the Earth was taken into account, while the bending of radar beams due to inhomogeneous refractivity was ignored. The calculation of simulated radar reflectivity along the beams was based on work by *Tong and Xue* [2005], and is a function of rain, snow, and

graupel. The simulated radial velocity, V_r, along the beams is a function of the averaged sedimentation speed (V_t) of hydrometeors (i.e., rain, snow, and graupel) and the three wind components from the nature run, which were mapped by rotating model coordinates back to the east-west (u), south-north (v), and z (w) directions, and is expressed as:

$$V_r = u\cos\alpha\sin\theta + v\cos\alpha\cos\theta + (w - V_t)\sin\alpha, \quad (1)$$

where α is the elevation angle and θ the azimuth angle of the radar beams. The simulated radial velocity is measured only if a precipitating cloud exists, with a minimum requirement of 5 dBZ reflectivity, and if the radar beam does not encounter terrain blockage. It was assumed that radars could reach a maximum range of 250 km, except for TEAM-R, which has a maximum range of 40 km due to its shorter electromagnetic wavelength (i.e., a higher dissipation rate). Data were sampled at the plan of position indicator (PPI), as in work by *Tong and Xue* [2005], and were then horizontally interpolated to a 2 km grid on regular Cartesian coordinates. This is the final product of simulated radar observations (both reflectivity and radial velocity) that was used for data assimilation experiments. Note that when assimilating radar radial velocity in the WRF Var system, the hydrometeors' sedimentation speed (i.e., V_t in equation (1)) was estimated from model values instead of from observed reflectivity (Q. Xiao, personal communication, 2008).

[18] In the data assimilation experiments, four CWB radars (R1–R4 in Figure 2) were fixed at their original locations. The S-POL radar was placed at 22.52°N and 120.43°E (R5 in Figure 2), and TEAM-R was placed at 22.88°N and 120.64°E (R6 in Figure 2).

2.3.2. Wind Profiler

[19] The heterogeneity of the refractivity index in the atmosphere due to variations of pressure, moisture, and temperature can result in a Doppler shift of dual electromagnetic waves. The backscattering of energy from irregularities in the refractive index due to turbulence (Bragg scattering) can be detected by wind profilers (i.e., ultrahigh frequency and very high frequency profiling radars), and its measurement is not restricted to the existence of precipitating clouds, light and heavy rain, and hail (Rayleigh scattering), as with weather radars mentioned above. In order to retrieve three dimensional wind components in the vertical direction, three beams are usually configured. One beam points in the vertical direction, while the other two point slightly to the east and south from vertical, with tilting angles of α and β, respectively. Both α and β were set to 21° in this study. Note that the bending of beams due to refractivity was again ignored.

[20] To retrieve three component winds, it was assumed that the local atmosphere was spherically symmetric with respect to the position of the wind profiler. The simulated radial velocities in the vertical (V_{rv}), off east (V_{re}), and off south (V_{rs}) directions are functions of u, v, and w as the following:

$$\begin{aligned} V_{rv} &= w, \\ V_{re} &= u \times \sin\alpha + w \times \cos\alpha, \\ V_{rs} &= -v \times \sin\beta + w \times \cos\beta. \end{aligned} \quad (2)$$

The three wind components, u, v, and w, can then be retrieved as the following, which were used in data assimilation experiments:

$$\begin{aligned} w &= V_{rv}, \\ u &= (V_{re} - V_{rv} \times \cos\alpha)/\sin\alpha, \\ v &= -(V_{rs} - V_{rv} \times \cos\beta)/\sin\beta. \end{aligned} \quad (3)$$

Wind profilers have two different observation modes, which can reach different heights with different resolutions. Although measurements can only reach about 5 km for the shorter observing distance, observations at this distance have a higher resolution in the lower atmosphere; thus, it was chosen for this study.

2.3.3. Surface Stations

[21] Thirty-three surface stations (black dots in Figure 2) were used in this study. With given latitudes and longitudes, hourly WRF outputs from the nature run were bilinearly interpolated to those observational sites.

2.3.4. Radiosondes

[22] Observations were simulated following radiosonde trajectories, which were drifted horizontally, using instantaneous outputs at exact hours from the nature run. Instruments started sampling data from the surface at the locations specified in Figure 2 and then drifted by the mean flow and instrument velocity (w_s; m s^{-1}) due to buoyancy. The trajectory of the radiosonde, S, was calculated as the following:

$$S = \sum_{t_0}^{t_f} \sqrt{u^2 + v^2 + (w + w_s)^2}\,\Delta t, \quad (4)$$

where Δt is the time interval of data sampling between two levels and was assigned to be 20 s. The vertical velocity of the instrument, w_s, was assumed to be 5 m s^{-1}. Data were collected up to the top of the model domain in the nature run. When assimilating radiosonde observations in WRF Var, soundings were treated as column data (i.e., no horizontal drifting).

2.3.5. Dropsondes

[23] As mentioned earlier, dropsonde soundings were simulated differently from the other observations. The algorithm was implemented into the WRF model and data were sampled during the integration of the nature run, instead of using instantaneous outputs. Similar to radiosondes, the simulations of dropsonde observations also followed the trajectories of those sondes (i.e., drifting horizontally). However, the absolute fall speed of the instruments (w_s; m s^{-1}) was a function of pressure and decreased when the pressure increased [*Hock and Franklin*, 1999], as shown in Figure 3, which was estimated from Figure 2 of *Hock and Franklin* [1999]. The fall speed, w_s, is expressed as:

$$w_s = -206.64 \times p^{-0.4076}, \quad (5)$$

where p is the pressure in hPa. The fall speed is slower in the lower atmosphere. As for radiosondes, no horizontal drifting

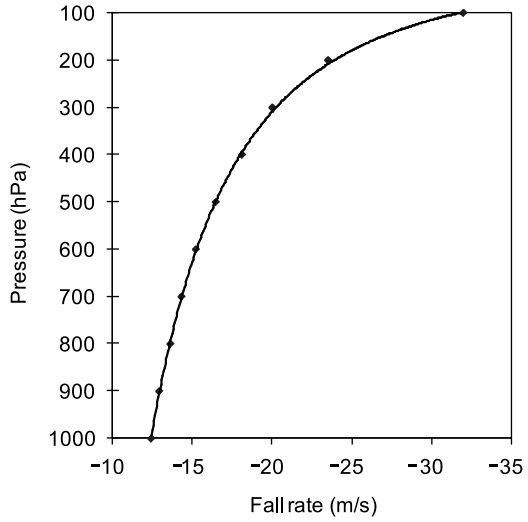

Figure 3. The fall speed of dropsondes as a function of pressure (estimated from Figure 2 of *Hock and Franklin* [1999]) used in the OSSE study.

was considered (i.e., treated as column data) when assimilating dropsonde soundings in WRF Var.

3. The Nature Run and Simulation of Observations

3.1. Case Study

[24] A northwest-southeast oriented frontal system (Figure 4a) that propagated from the north and passed over Taiwan on 6 and 7 June 2003 was chosen to examine the OSSE system. The simulation period chosen was from 0000 UTC 6 June to 0000 UTC8 June 2003, when the precipitation system was close to Taiwan, to ensure that simulated radar data were available for the data assimilation experiments. Heavy rainfall was observed in Taiwan from late 6 June to early 7 June. The maximum accumulated rainfall over southwestern Taiwan was more than 100 mm within 6 h, from 0000 UTC to 0600 UTC 7 June 2003 (Figure 4b), and this was the main rainfall period of interest for the data assimilation experiments. Note that a rainfall event in 2003, rather than one in 2008, was chosen because the OSSE system was developed and numerical experiments were conducted before TIMREX took place in 2008.

3.2. Model Configuration of the Nature Run

[25] Four domains with two-way interactions were configured for the WRF nature run (Figure 5). The resolutions for domains 1–4 were 27 km, 9 km, 3 km, and 1 km, respectively. The dimensions for each domain are given in Table 2. When doing an OSSE study, the simulation of radar data requires a high-resolution model simulation (i.e., a high-resolution nature run) due to the high resolution of the observations themselves in nature. Therefore, domain 4, which mainly covers Taiwan and its surrounding ocean, must be large enough to cover all radar scanning ranges.

[26] The Goddard Space Flight Center (GSFC) shortwave parameterization [*Chou and Suarez*, 1994], Rapid Radiative Transfer Model (RRTM) longwave parameterization [*Mlawer et al.*, 1997], Mellor-Yamada-Janjic (MYJ) boundary layer parameterization [*Janjic*, 1996], Purdue-Lin microphysics scheme [*Chen and Sun*, 2002], and Grell-Devenyi ensemble cumulus parameterization [*Grell and Devenyi*, 2002] were used (Table 3). The cumulus parameterization scheme was applied to domains 1 and 2 only. The model initial and boundary conditions were from Global Forecast System (GFS) reanalysis, which has a horizontal spatial resolution of 1° × 1°. The model integrated for two days, starting at 0000 UTC 6 June 2003 and a time step of 120 s for domain 1 was used. Domain 4 was mainly used to simulate all observations.

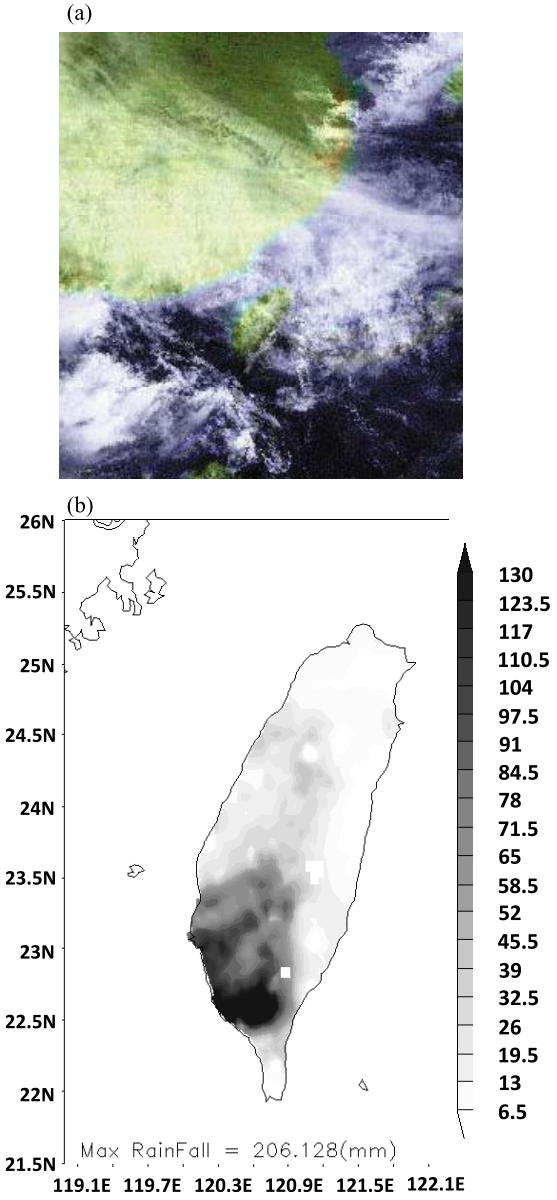

Figure 4. (a) Observed satellite image at 1200 UTC 6 June 2003 from Japan Geostationary Meteorological Satellite (GMS) in visible channels (courtesy of Kochi University, Japan), and (b) observed 6 h accumulated rainfall over Taiwan from 0000 UTC to 0600 UTC 7 June 2003.

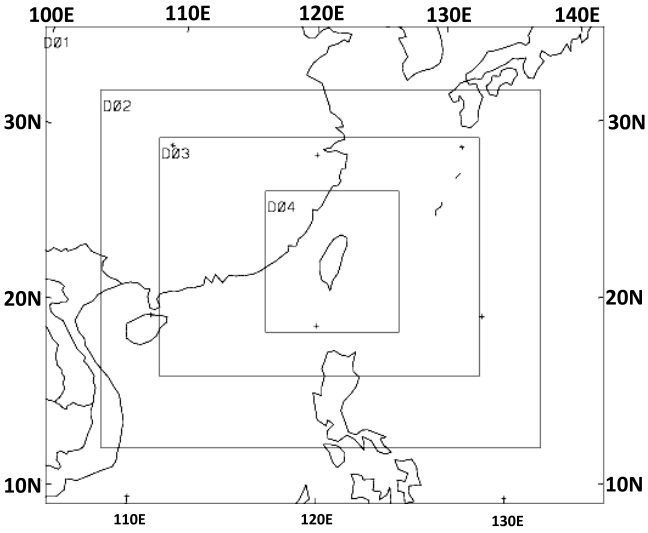

Figure 5. The nested domains used in the WRF nature run. Resolutions for domains 1, 2, 3, and 4 were 27 km, 9 km, 3 km, and 1 km, respectively.

However, for instruments that were outside domain 4, such as the radiosonde at Dongsha Island, domain 3 was used instead.

[27] For an OSSE study, the accuracy of the nature run compared with real observations usually is not a major concern as long as the nature run produces typical features of the phenomena of interest, such as fronts and heavy orographic rainfall in this study. However, since the first guess of data assimilation experiments in section 4 was from GFS reanalysis, instead of degraded fields from the nature run, the nature run should not be allowed to drift too much from the reanalysis, to prevent the impact of simulated observations on analysis and forecasts from being overestimated. Therefore, domain 1 in the nature run simulation was nudged to GFS reanalysis during the entire integration period using four dimensional data assimilation (FDDA).

3.3. Verification of Simulated Observations

[28] Most of the nature run results presented in this paper are from domain 3 because it has the same resolution as the highest resolution used in the data assimilation experiments in section 4. Figure 6 shows domain 3 results from the nature run after an 18 h integration. A southwesterly flow, typical during the monsoon season, was presented. A Mei-Yu front occurred over the Taiwan Strait approaching southern Taiwan, as indicated in the temperature gradient and wind shear. The surface front was located to the west of central Taiwan, while the 850 hPa one was shifted northward because the warm air mass from the south was above the cold air mass from the north. A weak, shallow, low-level cyclone was presented at the frontal zone and was located off the China coast. Strong convective systems, which were not embedded within the front, occurred east of Taiwan, on the western and southwestern coasts, and upstream of the southwesterly flow, as shown in the reflectivity field in Figure 6d.

Table 2. The Model Resolution and Grid Points in the x, y, and z Directions for Each Domain in the Nature Run and Data Assimilation Experiments

Domains (Resolution)	Nature Run (x, y, z)	Data Assimilation Experiments (x, y, z)
1 (27 km)	141 × 121 × 31	133 × 115 × 31
2 (9 km)	331 × 271 × 31	241 × 181 × 31
3 (3 km)	721 × 541 × 31	271 × 250 × 31
4 (1 km)	901 × 961 × 31	N/A

Table 3. Physics Schemes Used in the Nature Run and Data Assimilation Experiments

Physics Scheme	Nature Run	Data Assimilation Experiments
Microphysics	Purdue Lin	WSM 6-class graupel
Longwave/shortwave radiation	RRTM/Goddard	RRTM/Goddard
Cumulus parameterization	Grell-Devenyi ensemble	Kain-Fritsch
Boundary layer	Mellor-Yamada-Janjic TKE	YSU

[29] To evaluate the impact of radar data, the precipitation systems need to be close to Taiwan; therefore, the 6 h time period from 1800 UTC 6 June to 0000 UTC 7 June 2003 (18 h to 24 h integration of the nature run) was chosen for data assimilation. Figure 7 shows 5 km radar reflectivity and winds from the nature run and simulated observations at the S-POL station (i.e., R5 in Figure 2) at 1800 UTC 6 June 2003. The simulated radar reflectivity and radial wind velocity were very reasonable when compared with the nature run. Note that the observation errors were excluded in Figure 7 for the purpose of comparison between simulated radar observations and those from the nature run (i.e., verification of the radar simulator). With respect to the radar position, the strong convection bands at the east-northeast, the inflow from the west-southwest, and the outflow to the east-northeast were well simulated. The radar operator reasonably reproduced observations from the nature run. Other simulated observations from the nature run were also reasonable (figures not shown).

4. Data Assimilation Experiments

4.1. Experiment Design

[30] Figure 8 shows the flight track and the deployed locations of 15 simulated dropsondes that were used in this study. These dropsondes were released close to the island at the upstream end of the southwesterly monsoonal flow from an elevation of 14 km height. The detailed times and locations of the deployment are given in Table 4. Five data assimilation experiments were conducted to assimilate different simulated observations (Table 5). NONE, which did not assimilate any data, and GTS, which assimilated regular conventional radiosondes (i.e., soundings launched at 0000 UTC and 1200 UTC) and surface stations (i.e., hourly data), were included for comparison. Three observational strategies, SOP (Special Observation Period), IOP (Intensive Observation Period), and EOP (Extensive Observation Period) proposed in TIMREX 2008, with some modifications, were examined to investigate the impact of radar, dropsondes, and radiosonde frequency on analysis and short-term rainfall forecasts (Tables 1 and 5 and Figure 2). SOP differed from GTS by additionally assimilating hourly radar and wind profiler data

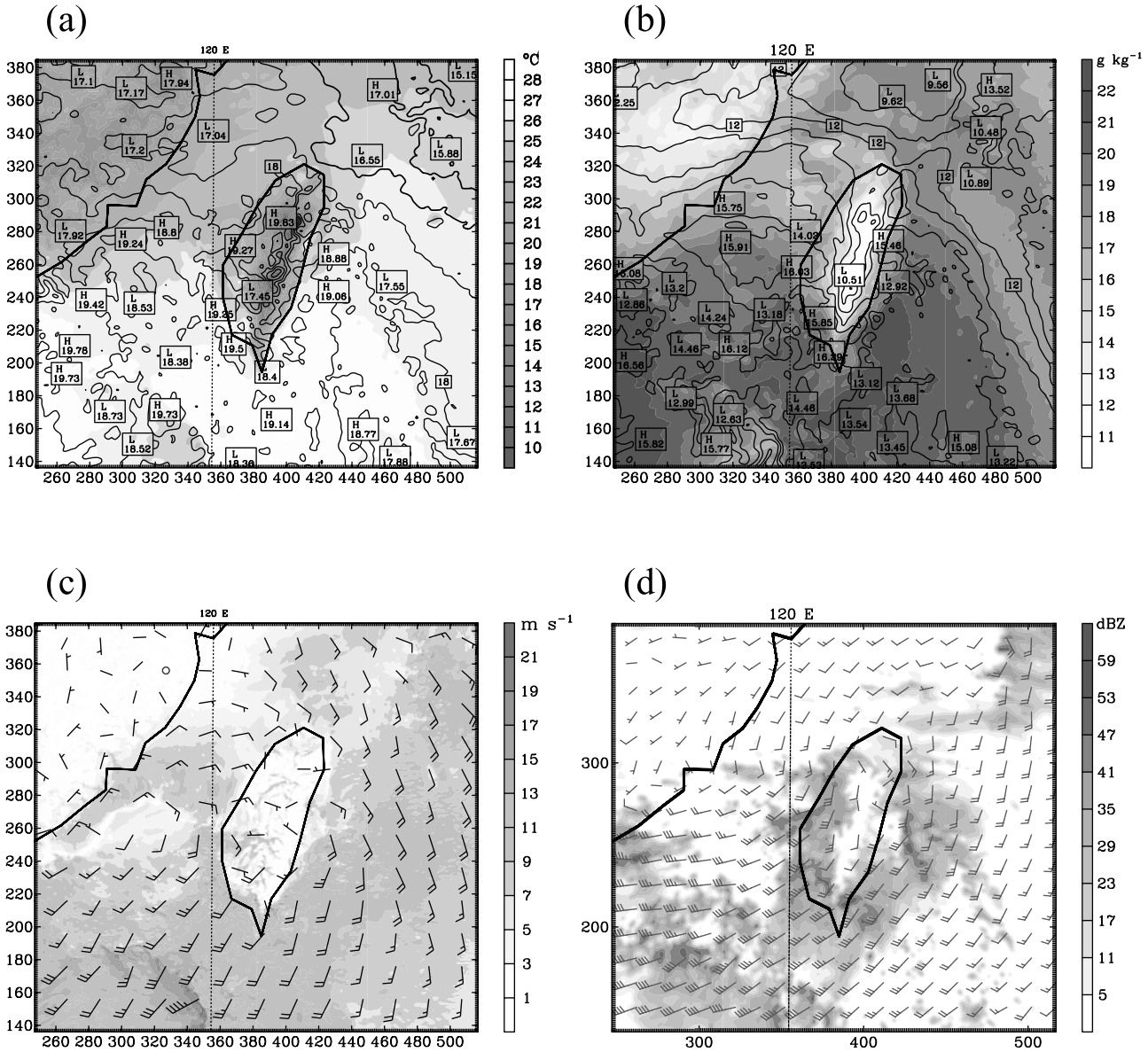

Figure 6. The first half level (shading) and 850 hPa (contour lines) (a) temperature (K) and (b) water vapor mixing ratio (g kg^{-1}), (c) the first half level wind speed (m s^{-1}; shading) and wind vectors, and (d) 850 hPa radar echo and wind vectors at 1800 UTC 6 June 2003 (18 h simulation) from domain 3 of the nature run.

from existing and additional stations; moreover, radiosonde launch frequency at regular sites and additional stations was every 6 h. IOP differed from SOP by adding dropsondes along the flight track in Figure 8. For EOP, radiosondes at all locations were launched every 3 h. The remaining observations in EOP were the same as those in IOP. Note that data sampling strategies for IOP and EOP in this study were slightly different from those in TIMREX. During TIMREX, for IOP, 6 out of 12 radiosonde stations launched sondes every 3 h, while the rest maintained the 6 h launch frequency; for EOP, radiosondes at all locations were launched every 3 h, except S9 and S10 (Figure 2), which were every 6 h. In the data assimilation experiments, data cycling was performed from 1800 UTC 6 June to 0000 UTC 7 June 2003 before 1 day forecasting. The assimilation of observations was performed at exact hours with a 1 h time window centered at the analysis time of three-dimensional variational data assimilation for all observations (i.e., analysis time ±0.5 h for data screening). The 1 h forecasted fields from the WRF model were used as the first guess of data assimilation during the data cycling, except at the initial time (i.e., 1800 UTC 6 June 2003), which used global reanalysis as the first guess. The same time step from the nature run (120 s) was used.

[31] Three WRF domains with two-way interactions were configured for the data assimilation experiments, as shown in Figure 9. The resolutions for domains 1 to 3 were 27 km, 9 km, and 3 km, respectively, and the grid dimensions are given in Table 2. YonSei University (YSU) boundary layer parameterization [*Hong et al.*, 2006], WRF single moment (WSM) 6-class graupel scheme [*Hong and Lim*, 2006], Kain-Fritch cumulus parameterization [*Kain*, 2004], GSFC

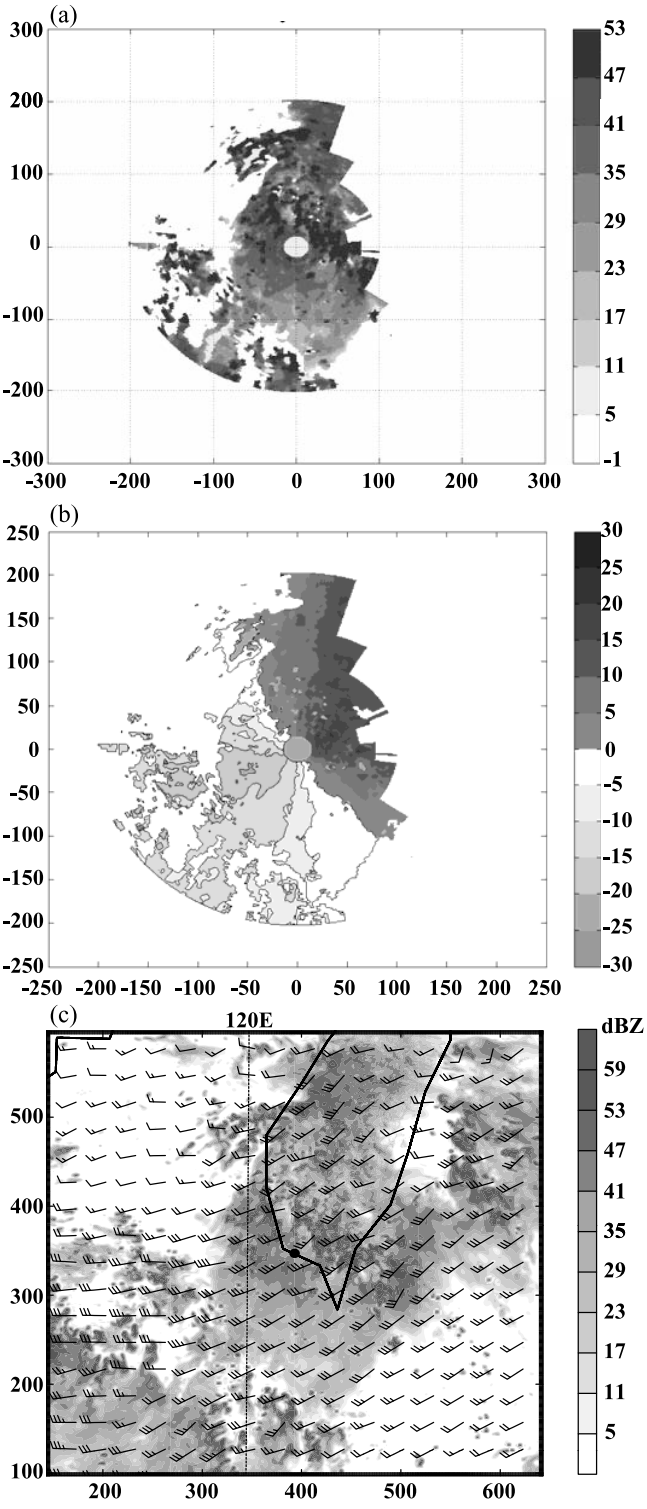

Figure 7. Simulated (a) reflectivity and (b) radial velocity ($m\ s^{-1}$) at 5 km height for the SPOL radar at 1800 UTC 6 June 2003. (c) The reflectivity at 5 km height and wind vectors from domain 4 of the nature run at the same time. The dot in Figure 7c indicates the location of the SPOL radar.

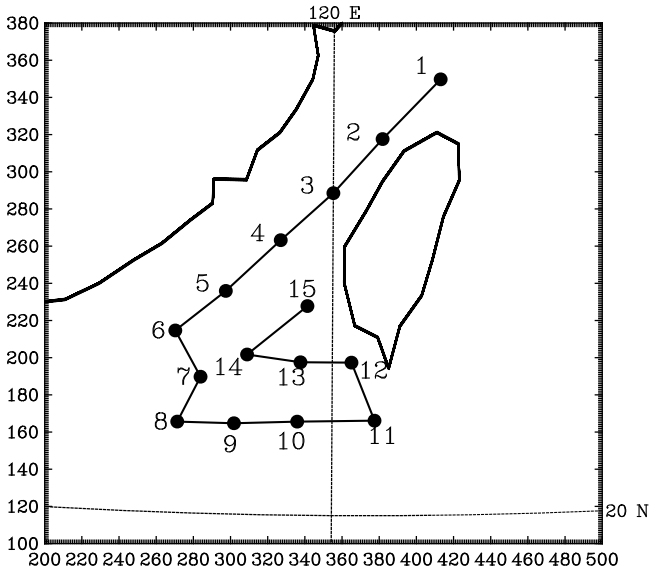

Figure 8. The flight track that was used in the data assimilation experiments. Dots indicate the locations where dropsondes were deployed and the numbers indicate the order of deployments. The dropsondes were released between 2030 UTC and 2300 UTC 6 June 2003.

shortwave scheme, and RRTM longwave scheme were used, all of which, except the radiation schemes, are different from those used in the nature run (Table 3) to reduce the likelihood of any identical twin problem. The cumulus parameterization scheme was applied to domains 1 and 2 only.

[32] Both the first guess at hour zero of data assimilation experiments and the boundary conditions for the data assimilation experiments were from GFS reanalysis. The first guess at 1800 UTC 6 June (Figure 10) was quite different from the nature run (Figures 6a–6c). The small-scale features in the nature run did not show up in the first guess due to the low resolution of the GFS reanalysis. Yet the synoptic and mesoscale features in the first guess were in some degree similar to, but still different from, those of the nature run. In the first guess, the front to the west of Taiwan was weaker and shifted southward, and the low pressure system off the

Table 4. The Locations and Times of Dropsonde Deployments on 6 June 2003 for the Flight Track in Figure 8

Dropsonde Number	Location (Latitude/Longitude)	Time of Deployment
1	25.990°N/121.659°E	2048 UTC
2	25.164°N/120.753°E	2109 UTC
3	24.411°N/120.000°E	2118 UTC
4	23.753°N/119.210°E	2127 UTC
5	23.038°N/118.401°E	2136 UTC
6	22.474°N/117.668°E	2144 UTC
7	21.853°N/118.062°E	2151 UTC
8	21.231°N/117.743°E	2157 UTC
9	21.231°N/118.570°E	2204 UTC
10	21.269°N/119.493°E	2212 UTC
11	21.288°N/120.621°E	2221 UTC
12	22.079°N/120.283°E	2229 UTC
13	22.079°N/119.530°E	2235 UTC
14	22.173°N/118.740°E	2242 UTC
15	22.850°N/119.624°E	2251 UTC

Table 5. Data Assimilation Experiment Design[a]

Experiment	Assimilated Observations
NONE	No observations
GTS	Radiosondes in 12 h sampling interval from existing stations only
	Hourly surface data from all 33 stations
SOP	Radiosondes in 6 h sampling interval from all existing and additional stations
	Hourly surface data from all stations
	Hourly radar data from existing and additional sites
	Hourly wind profiler from existing and additional sites
IOP	The same as SOP, except that dropsondes from the flight track in Figure 8 were included
EOP	The same as IOP, except that a 3 h sampling interval was used for all radiosondes

[a]Data cycling was performed from 1800 UTC June 6 to 0000 UTC June 7, 2003.

China coast was mislocated to the western coast of Taiwan. These differences resulted in quite different wind patterns over the Taiwan Strait between the nature run and the first guess of data assimilation experiments. For the first guess, warm and moist air did not intrude into the Taiwan area enough and winds to the southeast of Taiwan over the northeastern South China Sea had too great of a westerly component.

4.2. Data Assimilation Analysis

[33] Short-term rainfall forecast is the primary interest of this case study. Therefore, the discussion is mainly focused on the analysis of low-level wind and moisture, which are important variables to heavy rainfall events. Figure 11 shows wind speeds and vectors at the model first half level from the nature run and data assimilation experiments at 0000 UTC 7 June 2003. Compared with the nature run, without assimilating any observations (i.e., NONE at 6 h forecast), low-level winds were too weak at southwestern Taiwan, extending to the ocean, and were too strong over the ocean

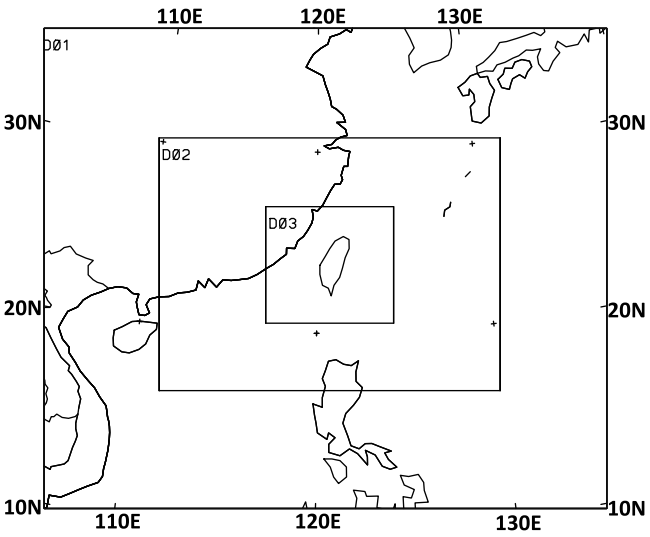

Figure 9. The nested domains used in data assimilation experiments. The terrain corresponds to the outer domain, domain 1. Resolutions are 27 km, 9 km, and 3 km for domains 1, 2, and 3, respectively.

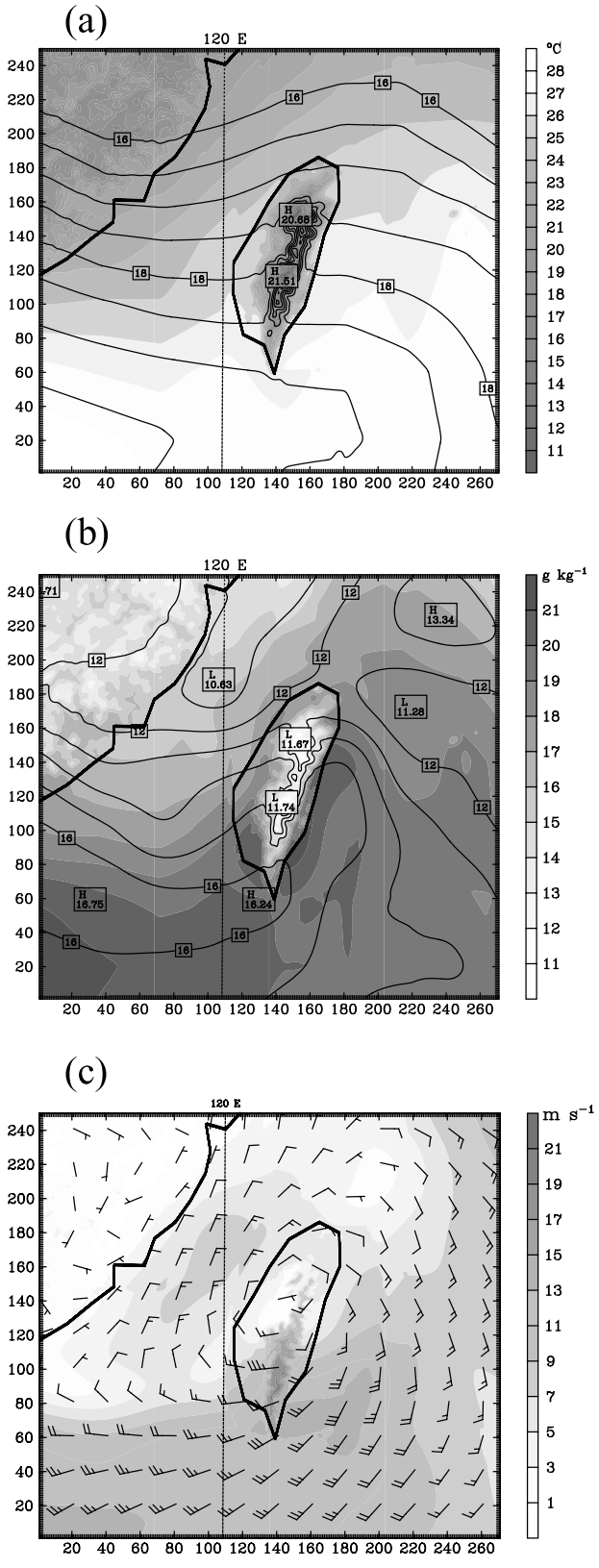

Figure 10. The first half level (shading) and 850 hPa (contour lines) (a) temperature (K) and (b) water vapor mixing ratio (g kg^{-1}) and (c) the first half level wind speed (m s^{-1}; shading) and wind vectors at 1800 UTC 6 June 2003 from GFS reanalysis, which were used as the background for data assimilation experiments.

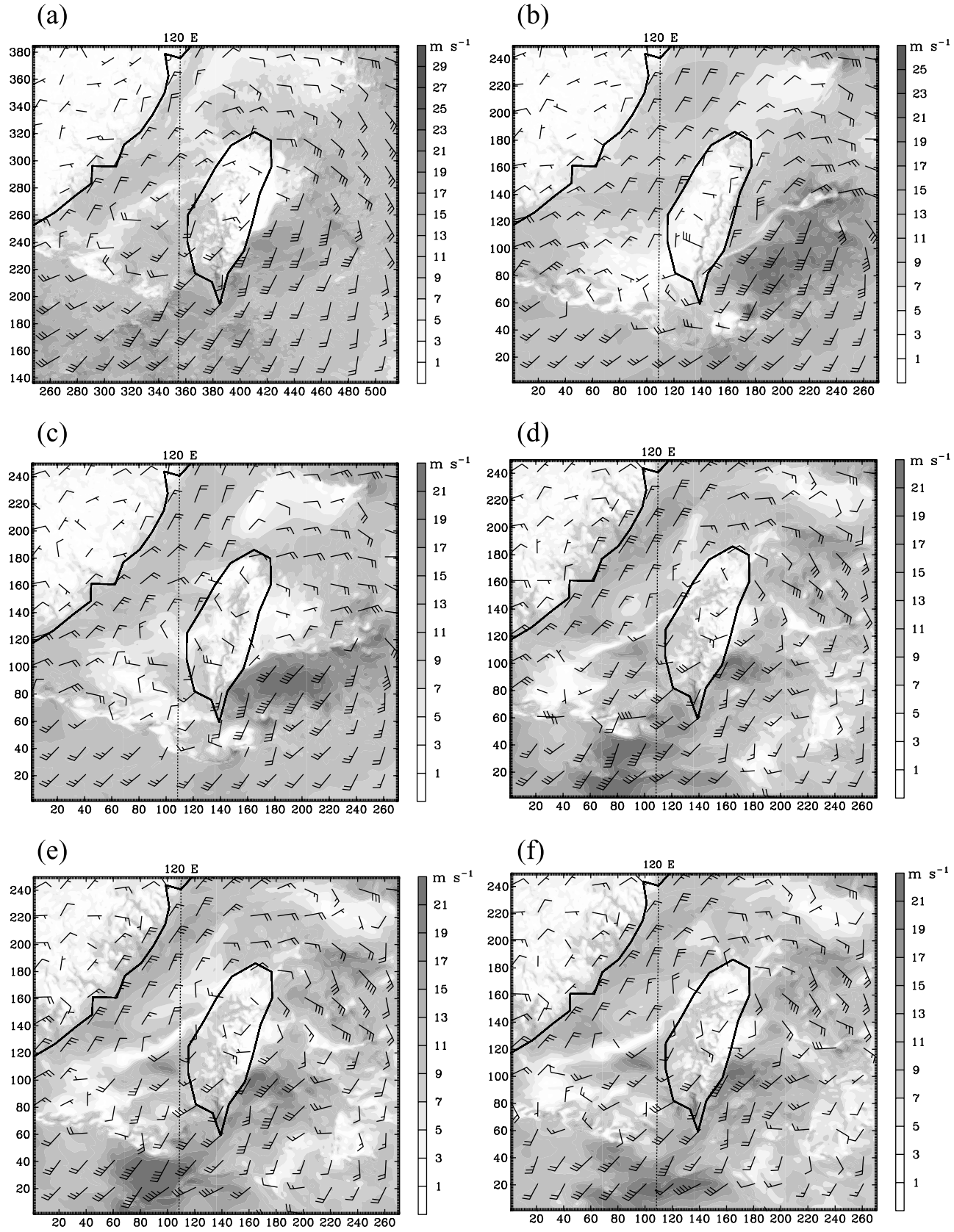

Figure 11. First model half level wind speed (m s^{-1}; shading) and vectors from (a) domain 3 of the nature run (24 h simulation), (b) NONE (6 h forecast), and analyses for (c) GTS, (d) SOP, (e) IOP, and (f) EOP at 0000 UTC 7 June 2003.

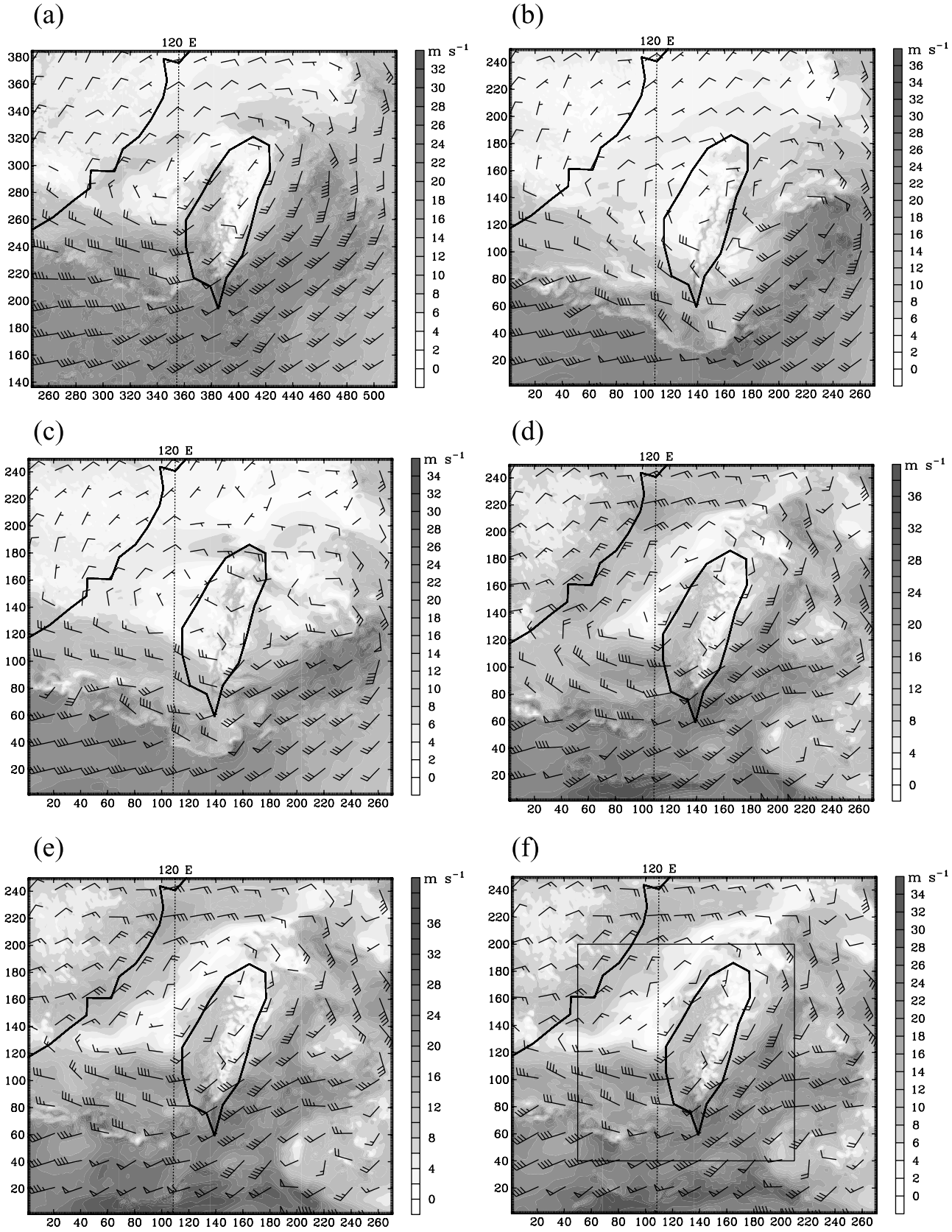

Figure 12. Same as Figure 11 but for 850 hPa plots. The square box in Figure 12f is the area for the calculation of root mean square errors (RMSEs) in Figure 13.

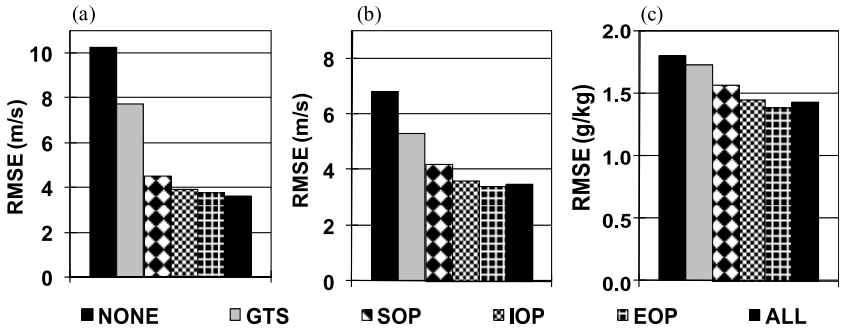

Figure 13. The root mean square errors (RMSEs) of analyses for 850 hPa (a) u (m s^{-1}), (b) v (m s^{-1}), and (c) vapor mixing (g kg^{-1}) at 0000 UTC 7 June from data assimilation experiments. The calculation area is the square box in Figure 12f.

off the southeast coast of Taiwan. These were slightly improved, in particular over the land, after the use of regular conventional data (i.e., GTS analysis), which included 4 radiosondes at 0000 UTC 7 June and 33 hourly surface stations. The use of radar and additional radiosondes/dropsondes (i.e., SOP, IOP, and EOP analysis) significantly improved modeled low-level winds over these two regions, as well as over the eastern coastal area. The improvement over the ocean off the southwest coast was due to the use of radar data and the upstream radiosondes (S11 in Figure 2). With the use of dropsondes (IOP versus SOP), the southwesterly monsoonal flow at low levels was slightly better organized in direction (Figure 11e versus 11d). It was unfortunate that the low-level jet over the northeastern South China Sea (i.e., close to the southern edge of the plotted domain in Figure 11) was too strong, where strong convective clouds occurred and neither radar data nor other observations were available in the low levels. This could result in the closure problem of the inappropriate lower boundary condition for radar data.

[34] Figure 12 shows wind information at 850 hPa at 0000 UTC 7 June 2003. Similar to the results for the surface wind, NONE produced the worst results, underestimating winds over western Taiwan due to the southward shift of the frontal zone and over the ocean near coastal regions in the southern half of Taiwan. Wind directions over these areas were also misrepresented, which could have an influence on orographic rainfall forecast. Moreover, the cyclonic circulation to the west of Taiwan was missing. The radiosonde sounding over Ma-Kung (S3 in Figure 2) in GTS slightly amended the situation, but improvement was limited. The underestimated wind speeds and inaccurate wind directions were significantly improved for SOP, IOP, and EOP. The problem of overestimated wind in low levels over the northeastern South China Sea in Figures 11d–11f still existed (Figures 12d–12f), but almost disappeared at higher levels (figure not shown), which received better coverage by radar data. The frontal zone region to the west of Taiwan (i.e., the weak wind zone along the front) was slightly improved after the use of dropsonde data (Figure 12d versus 12e). It was noticed that winds to the northwest of Taiwan, along the coastal region of China, became worse after the use of radar data. This resulted from the problem of partial data coverage by radar (i.e., data were only available near Taiwan due to the elevated scanning angle); a similar problem was reported by *Xue et al.* [2006]. This problem, again, greatly decreased with height due to the better coverage of radar data (figure not shown).

[35] To quantitatively evaluate results, the root mean square errors (RMSEs) of wind analyses at 0000 UTC 7 June 2003 were calculated from data assimilation experiments (Figures 13a and 13b) within the area of interest (the square box in Figure 12f), where there is a potential to influence rainfall in Taiwan. Since RMSEs of wind analyses at the surface from different experiments were qualitatively similar to those at 850 hPa, but with slightly smaller magnitudes, only results at 850 hPa are presented here. Errors of east-west (u) and south-north (v) wind components from NONE (i.e., 6 h forecast) were reduced 20–25% after the assimilation of regular conventional data (i.e., GTS). An additional reduction of errors by 17–32% resulted after the use of radar data and the higher frequency of radiosondes (SOP), in particular for the v wind component (~32%; Figure 13b). Regardless of the small differences, errors from IOP and EOP wind analyses, which assimilated dropsondes and more radiosondes, respectively, were slightly smaller than those from SOP.

[36] Figure 14 shows 850 hPa moisture analysis at 0000 UTC 7 June 2003. Compared to NONE, the assimilation of regular conventional data (i.e., GTS) gave slightly better moisture analysis, about 4% better (Figure 13c), mainly over land (Figure 14c). The use of more observations in SOP, IOP, and EOP further improved the 850 hPa moisture analysis (an additional 9–19% error reduction, Figure 13c), in particular over land, the front zone, and the south of Taiwan (Figures 14d–14f). The moist air over northwestern Taiwan was missing in all experiments, except EOP which was slightly better than the others. It was surprising to learn that the assimilation of more observations did not improve 2 m moisture analysis (figure not shown). This might be because errors in the first guess were comparable to observation errors (i.e., 10% relative humidity).

[37] It was noticed that the differences in wind and moisture analyses among SOP, IOP, and EOP were relatively small, in particular between IOP and EOP (Figures 11–14), implying that the information provided from IOP might be close to saturation by the temporal resolution. Therefore, extra radiosondes released at the same locations with a higher time frequency (i.e., every 3 h) did not provide much further information, suggesting that these soundings could

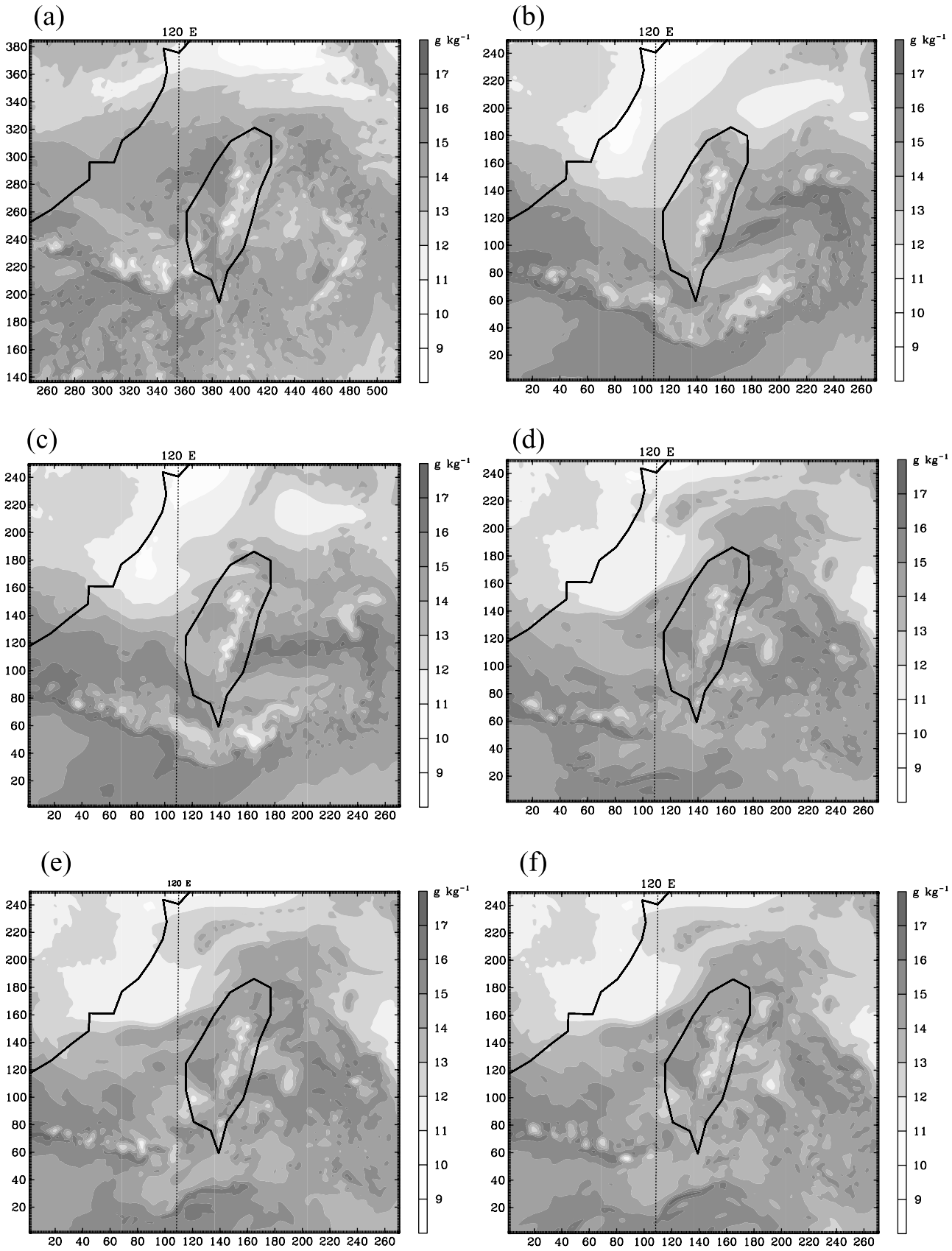

Figure 14. Same as Figure 11 but for 850 hPa water vapor mixing ratio (g kg^{-1}).

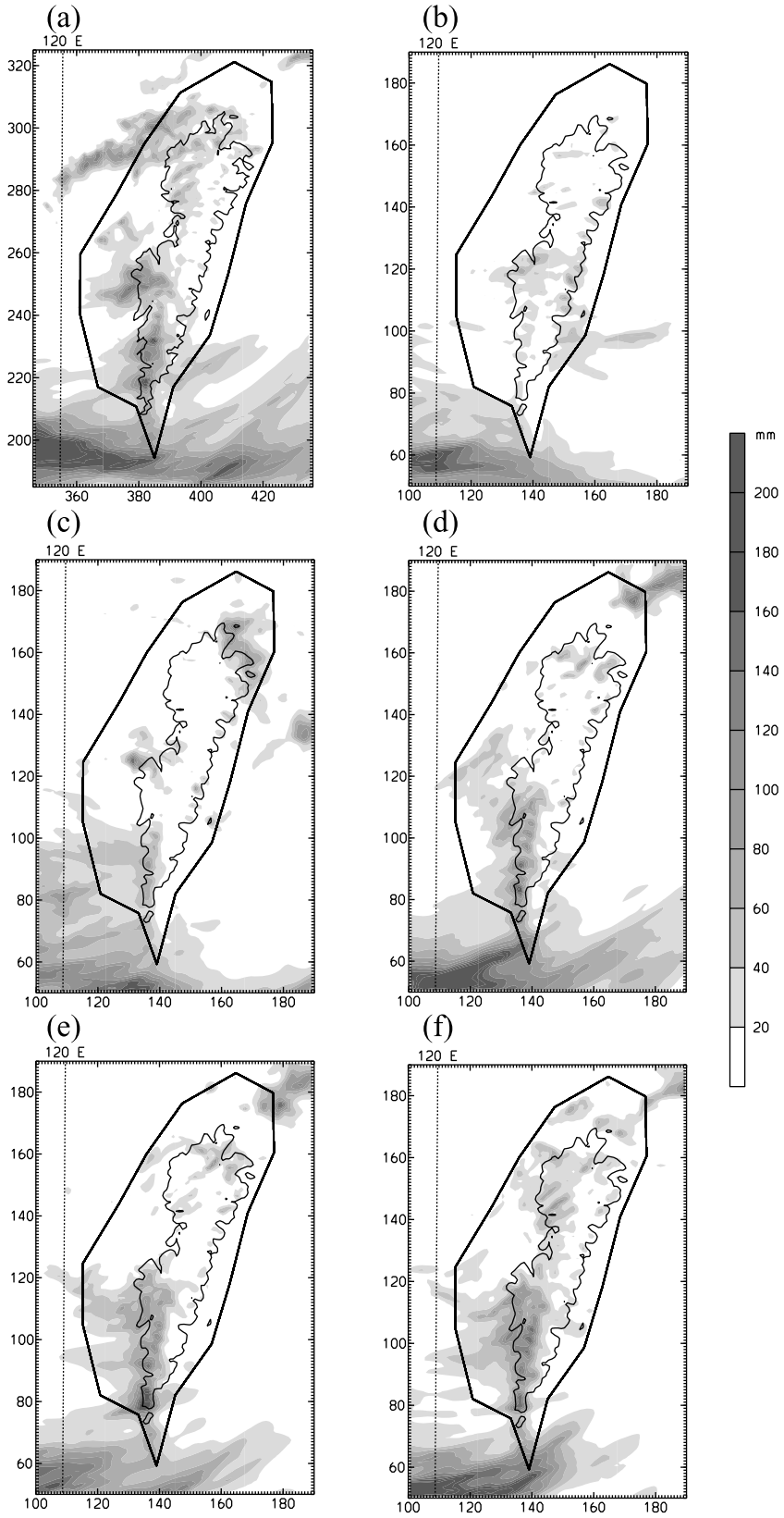

Figure 15. Six hour accumulated rainfall (mm) from 0000 UTC to 0600 UTC 7 June for (a) the nature run, (b) NONE, (c) GTS, (d) SOP, (e), IOP, and (f) EOP. The contour lines indicate an elevation of 1000 m.

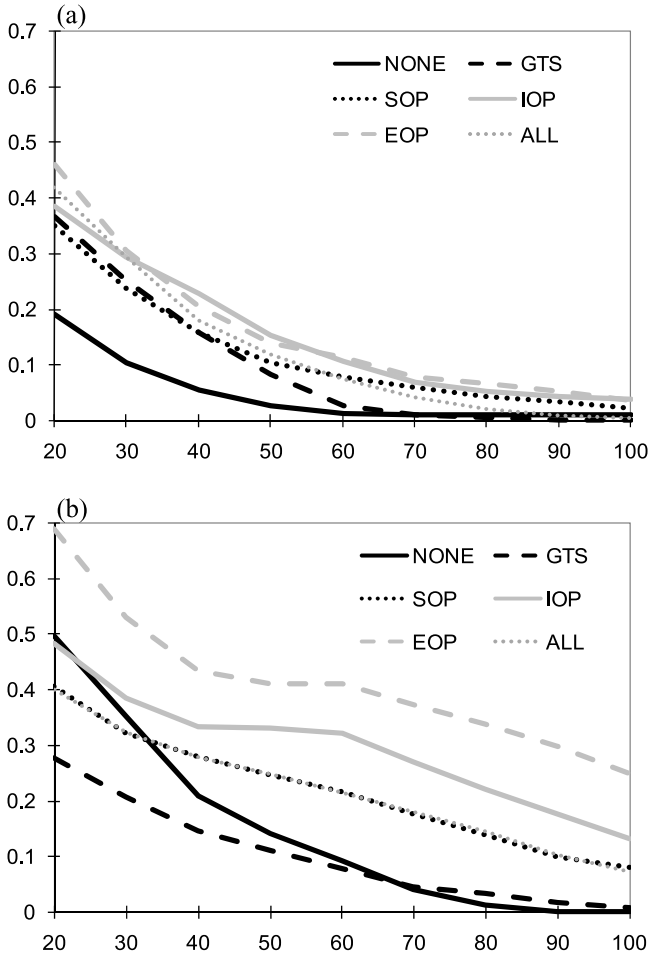

Figure 16. Six hour accumulated rainfall threat scores, from 0000 UTC to 0600 UTC 7 June with respect to different rainfall thresholds for elevations (a) below and (b) above 1000 m over Taiwan from different data assimilation experiments.

be deployed at different locations for better benefit (i.e., increased spatial resolution).

4.3. Short-Term Rainfall Forecast

[38] Six hour accumulated rainfall from 0000 UTC to 0600 UTC 7 June 2003 over the Taiwan area is shown in Figure 15. In the nature run, heavy rainfall occurred from middle to southern Taiwan on the windward side and mountain areas, and in northwestern Taiwan (Figure 15a); the maximum amount was more than 100 mm for 6 h accumulation. NONE missed most of the rainfall on the island, except producing light rainfall over the mountain region in central Taiwan. To quantitatively evaluate precipitation, threat scores (TSs) for the 6 h accumulated rainfall over Taiwan (i.e., land only) were also calculated (Figure 16) using the formula:

$$\mathrm{TS} = \frac{\mathrm{NH}}{\mathrm{NA} + \mathrm{NB} - \mathrm{NH}}, \tag{6}$$

where NH is the number of hits for a given rainfall threshold. NA and NB are the numbers of grid boxes whose rainfall amounts were greater than or equal to the given rainfall threshold from the nature run and data assimilation experiments, respectively. Scores were evaluated separately for regions with elevations below and above 1000 m (contour lines in Figure 15).

[39] In general, the threat scores decreased when the rainfall threshold increased (Figure 16). Over low elevation regions (Figure 16a), the scores for thresholds below 50 mm could be improved simply using conventional data due to the improvement on low level winds (Figure 11), but the rainfall area was too widespread (Figure 15c). To amend this overestimation of the occurrence of rainfall and to improve heavier rainfall forecasts in the southern half of Taiwan, radar data and additional radiosondes were required (SOP). Results from IOP and EOP were slightly superior to SOP due to the use of dropsondes (e.g., rainfall improved in central Taiwan) and extra radiosondes (Figure 16a).

[40] Over the high mountain regions (i.e., elevation greater than 1000 m), heavy rainfall was dominated by orographic lifting and moisture flux. The TS from NONE was slightly better than that from SOP for the threshold below 30 mm, but the score quickly dropped when the threshold increased. As the forecasted Mei-Yu front from NONE moved further south (Figure 12b), the impinging flow was shifted in direction (i.e., too much northerly wind component compared to the nature run and others), and rainfall was greatly underestimated (i.e., drier impinging flow). For experiments with fewer observations in categories, space, and/or time, such as upper air data in GTS, the mean flow might be partially recovered (Figure 12). However, some unrealistic convergence/divergence zones in data sparse areas or at the border of the data coverage areas could be introduced and this can potentially decrease rainfall scores (Figure 16b). After the use of more observational data in IOP and EOP, the southwesterly monsoonal flow was greatly improved, as was, to a lesser extent, the moisture at 850 hPa for the analyses. Therefore, rainfall over mountain regions from both experiments was better forecasted than in the other data assimilation experiments (Figures 15 and 16b), and the scores were also higher than those over the low elevation regions (Figure 16a). In particular, EOP produced a slightly better rainfall forecast over the northwestern mountain region due to the improved moisture analysis, in addition to improved low-level winds, near the region.

[41] To further investigate the frequency of radiosonde observations, another experiment was conducted, whose data sampling strategy was the same as EOP except that radiosondes at all locations were launched every hour (named ALL). It was surprising to see that wind and moisture analysis did not show better results when compared to IOP and EOP (Figure 13), and the TS scores were comparable to SOP (Figure 16), indicating that additional radiosondes from ALL (launched every hour) did not provide any benefit to rainfall forecasts.

[42] Unfortunately, there was no major rainfall over Taiwan after 0600 UTC 7 June 2003 and, therefore, no further rainfall comparisons could be made.

5. Concluding Remarks

[43] An Observing System Simulation Experiment (OSSE) was developed to study the impact of observational strategies in field experiments on weather analysis and

short-term forecasts. This study introduced the development of the OSSE system and presented some preliminary results. The observational operators (i.e., observation simulators) that were developed to simulate observations included radar, radiosonde, dropsonde, wind profiler, and surface stations.

[44] A heavy Mei-Yu rainfall event in June 2003 was chosen to demonstrate the practice of the OSSE technique using various observing strategies (i.e., SOP, IOP, and EOP), which were proposed for the Taiwan Island Monsoon Rainfall Experiment (TIMREX) field project in 2008, with some modifications. The nature run, a proxy atmosphere, was derived from a 1 km high-resolution Weather Research and Forecasting (WRF) model simulation. Observations were simulated using the nature run with random errors superimposed. Verification showed that simulated observations, such as radar reflectivity and radial velocity, were reasonably produced. As simulated observations were limited to Taiwan and its surrounding area, only short-term rainfall forecasts, as well as low-level winds and moisture analysis, were analyzed. A 6 h time period from 1800 UTC 6 June to 0000 UTC 7 June 2003 (i.e., 18 h to 24 h integration from the nature run), when convective systems were close to Taiwan, was chosen for data assimilation cycling. One day forecasts were performed afterward. To reduce the identical twin problem, most of the physics used in the nature run and data assimilation experiments were different, except for radiation. In addition, GFS reanalysis, instead of degraded fields from the nature run, was used for the first guess of data assimilation experiments in order to depart from the nature run.

[45] Results showed that the use of regular conventional data (i.e., GTS) slightly improved analysis in winds and, to a lesser extent, in moisture. The use of additional observations (i.e., SOP, IOP, and EOP) outperformed NONE and GTS. Over the low-elevation regions, the first 6 h rainfall forecast with the accumulated amount less than 50 mm was clearly improved using just regular conventional data. The use of more observations (e.g., SOP, IOP, and EOP) could slightly improve heavier rainfall forecast at low elevations, and significantly improve rainfall forecast at high elevations, in particular for EOP and, to a lesser extent, IOP. This is due to the great improvement on the southwesterly monsoonal flow after the assimilation of radar, dropsondes, and extra radiosondes.

[46] Comparisons between SOP and IOP (IOP and EOP) also showed that the use of dropsondes (additional radiosondes) slightly improved winds, such as the southwesterly monsoonal flow and the frontal zone to the west of Taiwan, and 850 hPa moisture, resulting in the improvement of orographic rainfall forecasts, in particular in central (northwestern) Taiwan. IOP, EOP, and ALL, which differed in the assimilation of radiosonde frequency (6 h, 3 h, and 1 h, respectively), as well as SOP, gave insignificant discrepancies or inconclusive discrepancies in rainfall patterns/scores, winds, and moisture over Taiwan and the surrounding areas, implying that the information provided by radiosondes in IOP gave very limited or no benefit. Observational errors, physics scheme errors (i.e., model errors), and the frequency of performing data assimilation all potentially contributed to the insignificant differences or inconclusive discrepancies. More studies on this are required.

[47] It should be pointed out that the simulation time period for experiments conducted in this study is relatively short. These experiments are useful for the verification of the OSSE system but are probably not sufficient to produce a robust recommendation, which requires a longer time simulation. For a long-term simulation, observations should be created over a larger area and the inclusion of satellite data may become important. In addition, the results presented here are based on one case with one set of random observational errors. The same case or different cases with different sets of random observational errors for longer time simulations should be performed in order to obtain statistical results for a more solid recommendation, in particular for the optimal frequency of launching radiosondes to avoid the saturation of information.

[48] While TIMREX was used to demonstrate the use of the OSSE system, the system can be easily applied to other existing field projects, such as hurricane field campaigns [*Aberson*, 2008; *Elsberry and Harr*, 2008; *Wu et al.*, 2005, 2007a, 2007b, 2009a, 2009b], to further examine observational strategies. The final goal is to apply this OSSE system to help design future field experiments and to test new locations for instrument installations. It should also be noted that any suggestion or recommendation from an OSSE study must be considered with caution because a simulation study can always depart from what happens in the real world, to some degree. Calibration experiments could be performed to learn the degree of this departure [*Lahoz et al.*, 2010; *Masutani et al.*, 2010] by comparing data assimilation results between the use of simulated observations versus real observations, to further examine the credibility of the system. Therefore, a follow-up study on the calibration experiments of the OSSE system (part 2) will be conducted in the near future.

[49] **Acknowledgments.** The authors would like to acknowledge the TIMREX project team, led by Wen-Chau Lee at NCAR and Jong-Dao Jou at National Taiwan University. We would also like to thank colleagues from Taiwan's National Typhoon and Flood Research Institute (NTFRI) for their help on this project and WRF development teams for their efforts on the model development. Thanks are extended to Steven Ghan, the editor of this manuscript, and three anonymous reviewers for their valuable scientific comments on the manuscript. The computational resources for all numerical simulations were provided by NTFRI. This work was supported by the National Science Council in Taiwan.

References

Aberson, S. D. (2003), Targeted observations to improve operational tropical cyclone track forecast guidance, *Mon. Weather Rev.*, *131*, 1613–1628, doi:10.1175//2550.1.

Aberson, S. D. (2008), Large forecast degradations due to synoptic surveillance during the 2004 and 2005 hurricane seasons, *Mon. Weather Rev.*, *136*, 3138–3150, doi:10.1175/2007MWR2192.1.

Atlas, R. A. (1997), Atmospheric observations and experiments to assess their usefulness in data assimilation, *J. Meteorol. Soc. Jpn.*, *75*, 111–130.

Bougeault, P., P. Binder, A. Buzzi, R. Dirks, J. Kuettner, R. Houze, R. B. Smith, R. Steinacker, and H. Volkert (2001), The MAP special observing period, *Bull. Am. Meteorol. Soc.*, *82*, 433–462, doi:10.1175/1520-0477(2001)082<0433:TMSOP>2.3.CO;2.

Brewster, K. A. (2003), Phase-correcting data assimilation and application to storm-scale numerical weather prediction. Part I: Method description and simulation testing, *Mon. Weather Rev.*, *131*, 480–492, doi:10.1175/1520-0493(2003)131<0480:PCDAAA>2.0.CO;2.

Chang, S. W., and T. R. Holt (1994), Impact of assimilating SSM/I rainfall rates on numerical prediction of winter cyclones, *Mon. Weather Rev.*, *122*, 151–164, doi:10.1175/1520-0493(1994)122<0151:IOASRR>2.0.CO;2.

Chen, S.-H., and W.-Y. Sun (2002), A one-dimensional time dependent cloud model, *J. Meteorol. Soc. Jpn.*, *80*, 99–118, doi:10.2151/jmsj.80.99.

Chou, M.-D., and M. J. Suarez (1994) An efficient thermal infrared radiation parameterization for use in general circulation models, *Tech. Rep. 104606*, 85 pp., NASA, Greenbelt, Md.

Daley, R., and T. Mayer (1986), Estimates of global analysis error from the global weather experiment observational network, *Mon. Weather Rev.*, *114*, 1642–1653, doi:10.1175/1520-0493(1986)114<1642:EOGAEF>2.0.CO;2.

Davis, C., et al. (2004), The bow-echo and MCV experiment: Observations and opportunities, *Bull. Am. Meteorol. Soc.*, *85*, 1075–1093, doi:10.1175/BAMS-85-8-1075.

Davolio, S., and A. Buzzi (2004), A nudging scheme for the assimilation of precipitation data into a mesoscale model, *Weather Forecast.*, *19*, 855–871, doi:10.1175/1520-0434(2004)019<0855:ANSFTA>2.0.CO;2.

Elsberry, R. L., and P. A. Harr (2008), Tropical cyclone structure (TCS0field 8) experiment science basis, observational platforms, and strategy, *Asia Pac. J. Atmos. Sci.*, *44*, 1–23.

Evans, A. G., J. D. Locatelli, M. T. Stoelinga, and P. V. Hobbs (2005), The IMPROVE-1 Storm of 1–2 February 2001. Part II: Cloud structures and the growth of precipitation, *J. Atmos. Sci.*, *62*, 3456–3473, doi:10.1175/JAS3547.1.

Garvert, M. F., B. A. Colle, and C. F. Mass (2005), The 13–14 December 2001 IMPROVE-2 Event. Part I: Synoptic and mesoscale evolution and comparison with a mesoscale model simulation, *J. Atmos. Sci.*, *62*, 3474–3492, doi:10.1175/JAS3549.1.

Garvert, M. F., B. Smull, and C. Mass (2007), Multiscale mountain waves influencing a major orographic precipitation event, *J. Atmos. Sci.*, *64*, 711–737, doi:10.1175/JAS3876.1.

Gelaro, R., T. E. Rosmond, and R. Daley (2002), Singular vector calculations with an analysis error variance metric, *Mon. Weather Rev.*, *130*, 1166–1186, doi:10.1175/1520-0493(2002)130<1166:SVCWAA>2.0.CO;2.

Grell, G. A., and D. Devenyi (2002), A generalized approach to parameterizing convection combining ensemble and data assimilation techniques, *Geophys. Res. Lett.*, *29*(14), 1693, doi:10.1029/2002GL015311.

Hock, T. F., and J. L. Franklin (1999), The NCAR GPS dropwindsonde, *Bull. Am. Meteorol. Soc.*, *80*, 407–420, doi:10.1175/1520-0477(1999)080<0407:TNGD>2.0.CO;2.

Hong, S.-Y., and J.-O. J. Lim (2006), The WRF single-moment 6-class microphysics scheme (WSM6), *J. Korean Meteorol. Soc.*, *42*, 129–151.

Hong, S.-Y., Y. Noh, and J. Dudhia (2006), A new vertical diffusion package with an explicit treatment of entrainment processes, *Mon. Weather Rev.*, *134*, 2318–2341, doi:10.1175/MWR3199.1.

Houze, R. A., and S. Medina (2005), Turbulence as a mechanism for orographic precipitation enhancement, *J. Atmos. Sci.*, *62*, 3599–3623, doi:10.1175/JAS3555.1.

Janjic, Z. I. (1996), The surface layer in the NCEP Eta model, paper presented at 11th Conference on Numerical Weather Prediction, Am. Meteorol. Soc., Norfolk, Va.

Jiang, Q., and J. D. Doyle (2004), Gravity wave breaking over the central Alps: Role of complex terrain, *J. Atmos. Sci.*, *61*, 2249–2266, doi:10.1175/1520-0469(2004)061<2249:GWBOTC>2.0.CO;2.

Kain, J. S. (2004), The Kain-Fritsch convective parameterization: An update, *J. Appl. Meteorol.*, *43*, 170–181, doi:10.1175/1520-0450(2004)043<0170:TKCPAU>2.0.CO;2.

Keil, M. (2004), Assimilating data from a simulated global constellation of stratospheric balloons, *Q. J. R. Meteorol. Soc.*, *130*, 2475–2493, doi:10.1256/qj.03.219.

Kuo, Y.-H., and R. A. Anthes (1984), Accuracy of diagnostic heat and moisture budgets using SESAME-79 field data as revealed by observing system simulation experiments, *Mon. Weather Rev.*, *112*, 1465–1481, doi:10.1175/1520-0493(1984)112<1465:AODHAM>2.0.CO;2.

Kuo, Y.-H., M. Skumanich, P. L. Haagenson, and J. S. Chang (1985), The accuracy of trajectory models as revealed by the observing system simulation experiments, *Mon. Weather Rev.*, *113*, 1852–1867, doi:10.1175/1520-0493(1985)113<1852:TAOTMA>2.0.CO;2.

Lahoz, W. A., R. Brugge, D. R. Jackson, S. Migliorini, R. Swinbank, D. Lary, and A. Lee (2005), An observing system simulation experiment to evaluate the scientific merit of wind and ozone measurements from the future SWIFT instrument, *Q. J. R. Meteorol. Soc.*, *131*, 503–523, doi:10.1256/qj.03.109.

Lahoz, W., B. Khattatov, and R. Menard (Eds.) (2010), *Data Assimilation, Making Sense of Observation*, 732 pp., Springer, New York.

Majumdar, S. J., S. D. Aberson, C. H. Bishop, R. Buizza, M. S. Peng, and C. A. Reynolds (2006), A comparison of adaptive observing guidance for Atlantic tropical cyclones, *Mon. Weather Rev.*, *134*, 2354–2372, doi:10.1175/MWR3193.1.

Masutani, M., et al. (2010), Observing system simulation experiments at the National Centers for Environmental Prediction, *J. Geophys. Res.*, *115*, D07101, doi:10.1029/2009JD012528.

Meng, Z., and F. Zhang (2007), Tests of an ensemble Kalman filter for mesoscale and regional-scale data assimilation. Part II: Imperfect model experiments, *Mon. Weather Rev.*, *135*, 1403–1423, doi:10.1175/MWR3352.1.

Mlawer, E. J., S. J. Taubman, P. D. Brown, M. J. Iacono, and S. A. Clough (1997), Radiative transfer for inhomogeneous atmospheres: RRTM, a validated correlated-k model for the longwave, *J. Geophys. Res.*, *102*, 16,663–16,682, doi:10.1029/97JD00237.

Neiman, P. J., P. O. G. Persson, F. M. Ralph, D. P. Jorgensen, A. B. White, and D. E. Kingsmill (2004), Modification of fronts and precipitation by coastal blocking during an intense landfalling winter storm in southern California: Observations during CALJET, *Mon. Weather Rev.*, *132*, 242–273, doi:10.1175/1520-0493(2004)132<0242:MOFAPB>2.0.CO;2.

Neiman, P. J., F. M. Ralph, A. B. White, D. D. Parrish, J. S. Holloway, and D. L. Bartels (2006), A multiwinter analysis of channeled flow through a prominent gap along the northern California coast during CALJET and PACJET, *Mon. Weather Rev.*, *134*, 1815–1841, doi:10.1175/MWR3148.1.

Palmer, T. N., R. Gelaro, J. Barkmeijer, and R. Buizza (1998), Singular vectors, metrics, and adaptive observations, *J. Atmos. Sci.*, *55*, 633–653, doi:10.1175/1520-0469(1998)055<0633:SVMAAO>2.0.CO;2.

Parrish, D. F., and J. C. Derber (1992), The National Meteorological Center's spectral statistical-interpolation analysis system, *Mon. Weather Rev.*, *120*, 1747–1763, doi:10.1175/1520-0493(1992)120<1747:TNMCSS>2.0.CO;2.

Ralph, F. M., et al. (1999) The California Land-falling Jets Experiment (CALJET): Objectives and design of a coastal atmosphere-ocean observing system deployed during a strong El Niño, paper presented at 3rd Symposium on Integrated Observing Systems, Am. Meteorol. Soc., Dallas, Tex.

Ralph, F. M., P. J. Neiman, and G. A. Wick (2004), Satellite and CALJET aircraft observations of atmospheric rivers over the eastern North Pacific Ocean during the winter of 1997/98, *Mon. Weather Rev.*, *132*, 1721–1745, doi:10.1175/1520-0493(2004)132<1721:SACAOO>2.0.CO;2.

Ralph, F. M., P. J. Neiman, and R. Rotunno (2005), Dropsonde observations in low-level jets over the northeastern Pacific Ocean from CALJET-1998 and PACJET-2001: Mean vertical-profile and atmospheric-river characteristics, *Mon. Weather Rev.*, *133*, 889–910, doi:10.1175/MWR2896.1.

Skamarock, W., J. Klemp, J. Dudhia, D. Gill, D. Barker, W. Wang, and J. Powers (2005) A description of the Advanced Research WRF version 2, *Tech. Note NCAR/TN-468+STR*, 100 pp., Natl. Cent. for Atmos. Res., Boulder, Colo.

Stoelinga, M. T., et al. (2003), Improvement of microphysical parameterization through observational verification experiment, *Bull. Am. Meteorol. Soc.*, *84*, 1807–1826, doi:10.1175/BAMS-84-12-1807.

Stoffelen, A., G. J. Marseille, F. Bouttier, D. Vasiljevic, S. de Haan, and C. Cardinali (2006), ADM-Aeolus Doppler wind lidar Observing System Simulation Experiment, *Q. J. R. Meteorol. Soc.*, *132*, 1927–1947, doi:10.1256/qj.05.83.

Tong, M., and M. Xue (2005), Ensemble Kalman Filter assimilation of Doppler radar data with a compressible nonhydrostatic model: OSS experiments, *Mon. Weather Rev.*, *133*, 1789–1807, doi:10.1175/MWR2898.1.

Warner, T. T., L. E. Key, and A. M. Lario (1989), Sensitivity of mesoscale-model forecast skill to some initial-data characteristics, data density, data position, analysis procedure and measurement error, *Mon. Weather Rev.*, *117*, 1281–1310, doi:10.1175/1520-0493(1989)117<1281:SOMFST>2.0.CO;2.

White, A. B., D. J. Gottas, E. T. Strem, F. M. Ralph, and P. J. Neiman (2002), An automated brightband height detection algorithm for use with Doppler radar spectral moments, *J. Atmos. Oceanic Technol.*, *19*, 687–697, doi:10.1175/1520-0426(2002)019<0687:AABHDA>2.0.CO;2.

Woods, C. P., M. T. Stoelinga, J. D. Locatelli, and P. V. Hobbs (2005), Microphysical processes and synergistic interaction between frontal and orographic forcing of precipitation during the 13 December 2001 IMPROVE-2 event over the Oregon Cascades, *J. Atmos. Sci.*, *62*, 3493–3519, doi:10.1175/JAS3550.1.

Wu, C.-C., et al. (2005), Dropwindsonde observations for typhoon surveillance near the Taiwan region (DOTSTAR): An overview, *Bull. Am. Meteorol. Soc.*, *86*, 787–790, doi:10.1175/BAMS-86-6-787.

Wu, C.-C., J.-H. Chen, P.-H. Lin, and K.-H. Chou (2007a), Targeted observations of tropical cyclone movement based on the adjoint-derived sensitivity steering vector, *J. Atmos. Sci.*, *64*, 2611–2626, doi:10.1175/JAS3974.1.

Wu, C.-C., K.-H. Chou, P.-H. Lin, S. D. Aberson, M. S. Peng, and T. Nakazawa (2007b), The impact of dropwindsonde data on typhoon track forecasts in DOTSTAR, *Weather Forecast.*, *22*, 1157–1176, doi:10.1175/2007WAF2006062.1.

Wu, C.-C., S.-G. Chen, J.-H. Chen, K.-H. Chou, and P.-H. Lin (2009a), Interaction of typhoon Shanshan (2006) with the midlatitude trough from both adjoint-derived sensitivity steering vector and potential vorticity perspectives, *Mon. Weather Rev.*, *137*, 852–862, doi:10.1175/2008MWR2585.1.

Wu, C.-C., et al. (2009b), Inter-comparison of targeted observation guidance for tropical cyclones in the North western Pacific, *Mon. Weather Rev.*, *137*, 2471–2492, doi:10.1175/2009MWR2762.1.

Xue, M., M. Tong, and K. K. Droegemeier (2006), An OSSE framework based on the ensemble square root Kalman Filter for evaluating the impact of data from radar networks on thunderstorm analysis and forecasting, *J. Atmos. Oceanic Technol.*, *23*, 46–66, doi:10.1175/JTECH1835.1.

Yu, C.-K., D. P. Jorgensen, and F. Roux (2007), Multiple precipitation mechanisms over mountains observed by airborne Doppler radar during MAP IOP5, *Mon. Weather Rev.*, *135*, 955–984, doi:10.1175/MWR3318.1.

W.-Y. Chang, J.-Y. Chen, and P.-L. Lin, Department of Atmospheric Sciences, National Central University, Chung-Li 320, Taiwan.

S.-H. Chen, Department of Land, Air, and Water Resources, University of California, One Shields Avenue, Davis, CA 95616, USA. (shachen@ucdavis.edu)

P.-H. Lin, Department of Atmospheric Sciences, National Taiwan University, Taipei 106, Taiwan.

W.-Y. Sun, Department of Earth and Atmospheric Sciences, Purdue University, West Lafayette, IN 47907, USA.